VIII International Conference on Fracture Mechanics of Concrete and Concrete Structures
FraMCoS-8
J.G.M. Van Mier, G. Ruiz, C. Andrade, R.C. Yu and X.X. Zhang (Eds)

A TWO-SCALE (FEM-DEM) APPROACH FOR CONCRETE

M. NITKA[*], Ł. SKARŻYŃSKI[*] AND J. TEJCHMAN[*]

[*] Gdansk University of Technology
Narutowicza 11/12, 80-233 Gdańsk-Wrzeszcz, Poland
e-mail: micnitka@pg.gda.pl, lskarzyn@pg.gda.pl, tejchmk@pg.gda.pl

Key words: concrete, Digital Image Correlation (DIC), Discrete Element Method (DEM), Finite Element Method (FEM), Fracture Process Zone (FPZ), Meso-structure, Two-scale approach

Abstract: A two-scale numerical homogenization scheme for a description of the 2D behaviour of concrete under bending was proposed. At the meso-level, concrete was described with the discrete method (DEM), and at the macro-level with the finite element method (FEM). The average stress response of a discrete micro-structure was obtained in each macroscopic Gauss point of the FE mesh as the result of the macroscopic deformation history imposed on the representative volume element (RVE). Discrete element simulations were performed with concrete specimens under compression and tension. In addition, three-point bending laboratory tests were carried out on notched concrete beams of a different size wherein the influence of the mix type, aggregate shape, volume of aggregate, aggregate size and sieve curve was investigated. The width and shape of a fracture process zone (FPZ) and crack width were measured using the digital image correlation (DIC) technique.

1 INTRODUCTION

To realistically capture the fracture behaviour of concrete, its micro-structure should be taken into account. However, when modelling micro-structure using FEM, a huge number of finite elements and computational effort are required. To practically solve this problem, multi-scale computational homogenization approaches are applied which are aimed at calculations of material properties at a global level using the data from different lower material levels. In a two-scale approach [1], the material behaviour is simultaneously studied at two scales: 1) at the meso-level, where the material micro-structure is considered and 2) at the macro-level, where the material is treated as a homogeneous one. The modelling procedure computes a stress-strain relationship at every integration point of the macro-structure by detailed calculations of micro-structure attributed to that point. Thus, any constitutive assumption at the macro-level is not needed.

Our paper considers a two-scale numerical homogenization scheme for a description of the 2D behaviour of concrete beams under bending. At the micro-level, the structure was described with the discrete method (DEM) by assuming rigid interacting discs with contact moments and cohesion [2]. At the macro-scale level, a numerical solution was obtained with the finite element method (FEM) with the aid of the tangent stiffness matrix calculated directly from a discrete concrete behaviour. The average stress response of discrete micro-structure was obtained in each macroscopic Gauss point of the FE mesh as the result of the macroscopic deformation history imposed on the representative volume element (RVE). In addition, the acoustic tensor was calculated at the Gauss points [1], which is the best indicator for the unstable material behaviour [3].

In parallel, comparative three-point bending laboratory tests were carried out on notched

concrete beams of a different size [4], [5]. The influence of the mix type, aggregate shape, aggregate volume, aggregate size and aggregate distribution was investigated. The width and shape of both a fracture process zone (FPZ) and crack above the notch were measured using a digital image correlation (DIC) technique which is an optical way to visualize surface displacements by successive post-processing of digital images taken at a constant time increment from a professional digital camera [4]. In addition, a size effect phenomenon was experimentally investigated.

2 TWO-SCALE FORMULATION

2.1 Meso-scale formulation

The concrete at the meso-scale was simulated as a set of N polydisperse discs, with diameters between 0.5 mm and 16 mm. All grains interact via linearly elastic normal and tangential Mohr-Coulomb law [6] with cohesion: the normal contact force f_n is related to the normal interpenetration δ of the contact as $F^n = k^n \delta$, where k^n is the normal stiffness coefficient. The tangential component F^s of the contact force is proportional to the tangential elastic relative displacement with the tangential stiffness coefficient k^s. The Mohr-Coulomb (fig.1) condition $|F^s| < F^s{}_{\max} + |F^n| tg\mu$ and $|F^n| > F^n{}_{\min}$ requires an incremental evaluation of F^s in each step ($F^s{}_{\max}$ is cohesion, $F^n{}_{\min}$ is the tensile resistance and μ is the inter-particle friction angle). A normal viscous component opposing the relative normal motion of any pair of grains in contact was added to the elastic force F^n to obtain a critical damping of the dynamic system when equilibrium states were computed.

2.2 Macro-scale formulation

A quasi-static finite strain continuum formulation was considered at the macroscopic level. The constitutive response at this level was obtained directly from DEM computations in the representative element volume (REV). For a given history of the macroscopic deformation gradient $\boldsymbol{F}$, the macroscopic Cauchy stress $\boldsymbol{\sigma}$ resulted from microscopic grain forces through the formula written in terms of the Piola-Kirchhoff stress $\mathbf{P}$.

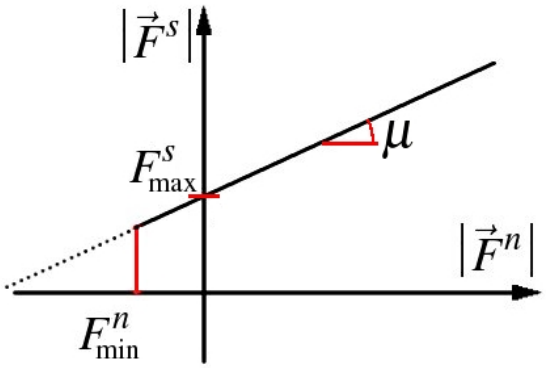

Figure 1: Mohr-Coulomb's law assumed for discrete calculations.

The effective constitutive behaviour was formally expressed as

$$\bar{\mathbf{P}}(t) = \Gamma^t\{\bar{\mathbf{F}}(\tau), \tau \in [0,t]\}. \quad (1)$$

We assumed that for any given history of $\mathbf{F}$ till time t, $\mathbf{P}(t)$ admitted the right time derivative

$$\dot{\bar{\mathbf{P}}} = lim_{\delta t \to 0} \frac{\bar{\mathbf{P}}(t+\delta t) - \bar{\mathbf{P}}(t)}{\delta t} \quad (2)$$

and that the right-sided derivative $\dot{\bar{\mathbf{P}}}$ depended on the right time derivative $\dot{\bar{\mathbf{F}}}$ only that is

$$\dot{\bar{\mathbf{P}}} = \Psi(\dot{\bar{\mathbf{F}}}). \quad (3)$$

The function Ψ is generally non-linear with respect to its argument $\dot{\bar{\mathbf{F}}}$. For a given rate of the deformation gradient $\boldsymbol{F}^0$, assuming that Ψ is differentiable at $\boldsymbol{F}^0$, one could determine the material tangent moduli as

$$D_{iJkL}\left(\dot{\bar{\mathbf{F}}}^0\right) = \frac{\partial \Psi_{iJ}}{\partial \dot{\bar{F}}_{kl}}\Big|_{\dot{\bar{\mathbf{F}}}=\dot{\bar{\mathbf{F}}}^0}, \quad (4)$$

where the capital indices refer to Lagrangian variables and small indices refer to Eularian ones, respectively.

At the macroscopic scale, finite elements were employed to solve the homogenized problem. When an incremental linearization

procedure was adopted for the obtained non-linear problem, the constitutive function Ψ and its derivatives were evaluated numerically in each integration (Gauss) point. During each time step, from t to $t+\Delta t$, in every Gauss point, the increment of the deformation gradient $\Delta \mathbf{F}=\dot{\overline{\mathbf{F}}}\,\Delta t$ was transmitted to the microstructure. As the result of DEM computations, the Piola-Kirchhoff stress $\overline{\mathbf{P}}(t+\Delta t)$ was returned to each Gauss point and the corresponding stress rate was computed as

$$\Psi(\dot{\overline{\mathbf{F}}}) = \frac{\overline{\mathbf{P}}(t+\Delta t) - \overline{\mathbf{P}}(t)}{\Delta t}, \qquad (5)$$

giving the discrete version of the constitutive function Ψ in Eq.3. A second step in the integration procedure at the level of a macroscopic Gauss point concerned the computation of the material tangent moduli D_{iJkL} needed in a typical Newton-Raphson algorithm. Since the derivatives in the Eq.4 involve the function Ψ which is itself computed as a derivative in Eq.5, the tangent moduli should be computed in two steps. For the given $\dot{\overline{\mathbf{F}}}$, we first computed $\Psi_{iJ}(\dot{\overline{\mathbf{F}}})$ (Eq.5). This corresponded to the increment of deformation gradient $\Delta \mathbf{F}=\dot{\overline{\mathbf{F}}}\,\Delta t$. Then, we considered the perturbed increments of the deformation gradient $\Delta F^*_{kL} = \Delta F_{kL} + \varepsilon \Delta t \Delta^{kL}$, where Δ^{kL} is the second-order (two-point) tensor such that all its components were equal to 0 except the kL one which was equal to 1, and ε was a small perturbation parameter. Following again Eq.5, we computed $\Psi_{iJ}{}^{d}(\dot{\overline{\mathbf{F}}}_{kL} + \varepsilon\Delta^{kL})$. Next the computations were performed for all different values of k and L (i.e. 4 computations in 2D case). Finally, the results of these two steps allowed for the computation of the material tangent moduli

$$D_{iJkL} = \frac{\Psi^{d}{}_{iJ}(\dot{\overline{\mathbf{F}}}_{kL} + \varepsilon\Delta^{kL}) - \Psi^{d}{}_{iJ}(\dot{\overline{\mathbf{F}}}_{kL})}{\varepsilon} \qquad (6)$$

as a discrete version of Eq.4. This procedure was performed in each time step and in each Gauss point of the macroscopic finite element discretization. The RVE size was calculated according to the procedure described by Skarżyński and Tejchman [7].

3 TWO-SCALE RESULTS

The combined FEM-DEM method was implemented in the FEM code *'FlagsHyp'* [8] that involved several significant code modifications. For the initial tests, the 2D quadratic element with four Gauss points was chosen. A very simple mesh with 4 elements was used. At the microscopic level, in DEM calculations, the number of aggregate grains in the REV cell was 400 in order to reduce the computation time. According to the stability studies [9], the variation step f=0.1 and perturbation ε=2e-5 where chosen. The two-scale tests were performed without cohesion between grains. Initially, REV was assigned an isotropic stress state by compression at the mesoscopic scale under a kinematic control up to a certain stress. Accordingly, the stress state at the integration point in the FE element was equal to the microscopic stress. An initial two-scale numerical test was performed by modelling a typical laboratory biaxial compression test with free dilatancy of a pure aggregate specimen (concrete without cohesion). A constant pressure σ_0 was applied to lateral sides, while the top was displaced downward. Using the symmetry of the problem, only the upper left quarter of the specimen is taken into account. The case with a smooth bottom in Fig.2 shows typical a biaxial compression response with hardening, peak and softening on the stress-strain curve and volumetric strain curve exhibiting initially small contractancy and then strong dilatancy. The calculated results from the two-scale FEM-DEM analysis are similar to pure discrete ones. In turn, the response of the specimen in the case with a frictional bottom is significantly perturbated on the specimen ends (the lower and earlier peak stress and delayed dilatancy) and departs evidently from the pure discrete response. This was expected, since the latter belongs definitely to a heterogeneous boundary value problem at the macroscopic

scale and differs essentially from the elementary response given by the DEM.

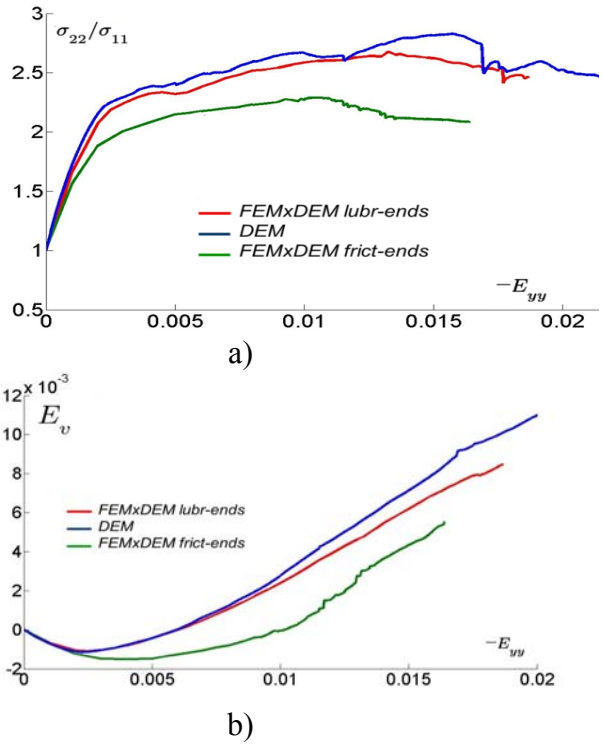

Figure 2: Stress-strain curves (a) and volume changes (b) from comparative two-scale computations and discrete calculations during biaxial compression test.

4 DISCRETE RESULTS FOR CONCRETE USING DEM

First, the numerical 2D calculations (using the program YADE (Kozicki and Donze [10], Kozicki et al. [11]) were carried out with typical quasi-static laboratory tests for concrete: uniaxial compression and uniaxial tension. During compression, the specimens 10×10 cm^2 were analyzed (Fig.3a). In turn, during tension the specimens in the form of so-called 'dog-bones' were used (height 15 cm, bottom and top width 10 cm and mid-part width 6 cm (Fig.3b). The aggregate shape was circular , its area was 55% and its range varied between 0.5 mm and 16 mm. The Poisson's ratio and Young's modulus of the grain contact were taken as ν=0.2 and E=380 GPa, respectively.

The discrete results of uniaxial compression were compared to the experiments by van Mier [12] (Figs.4a and 5a). In turn, the discrete results of uniaxial tension were compared to the experiments by van Vliet and van Mier [13] (Figs.4b and 5b). The numerical cohesion was taken as 2.5 MPa and tensile resistance 1.25 MPa (compression), and 1.0 MPa and 0.5 MPa (tension), respectively.

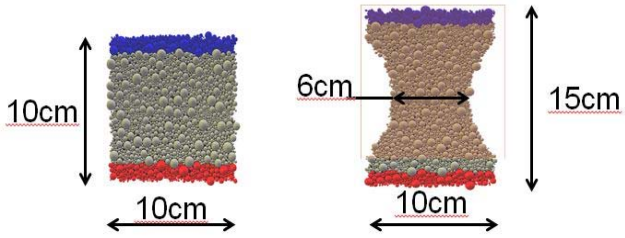

Figure 3: Geometry of concrete specimens under uniaxial compression and tension.

A satisfactory agreement between calculations and experiments was achieved with respect to the stress-strain curve and specimen fracture (vertical cracks during compression and horizontal cracks during tension).

Figure 6 demonstrates the effect the aggregate distribution in concrete with the compressive strength of about 15 MPa. The minimum aggregate diameter was 2 mm, 1 mm and 0.5 mm, whereas the maximum aggregate diameter was 16 mm (mean aggregate diameter d_{50} was 4.5 mm, 4 mm and 3 mm). The calculated strength and material ductility increase with increasing mean aggregate diameter.

The influence of the loading velocity on the dynamic macroscopic stress-strain diagram for concrete with the compressive strength of about 15 MPa is depicted in Fig.7 (the vertical loading velocity varied between 0.0025 mm/s and 25 mm/s). During dynamic uniaxial compression (Fig.7a), the strength and material ductility increased with increasing loading velocity that was in agreement with laboratory tests. However, during dynamic uniaxial tension (Fig.7b), this effect did not occur that was opposite to experiments. This problem merits further investigations.

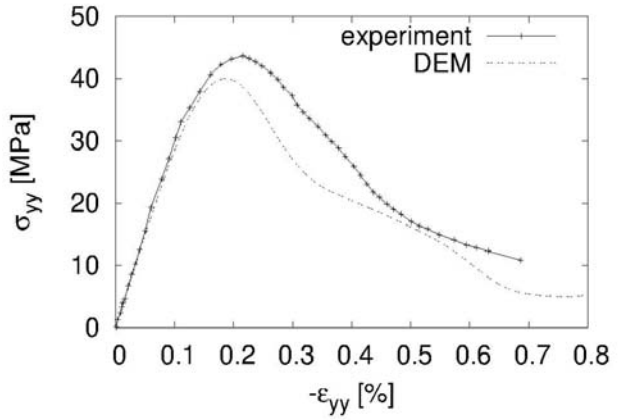

a)

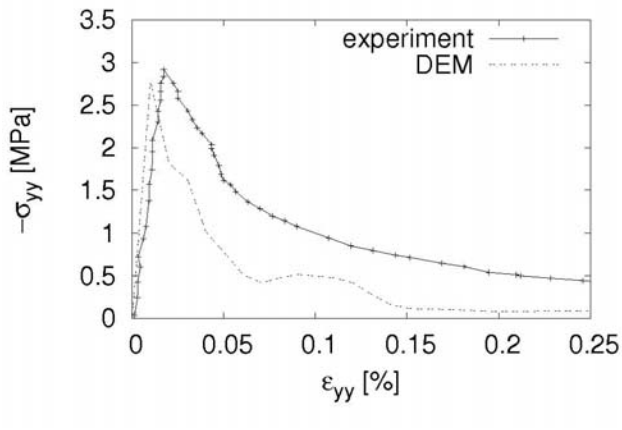

b)

Figure 4: Comparison between discrete calculations and experiments [12], [13] during uniaxial compression (a) and uniaxial tension (b).

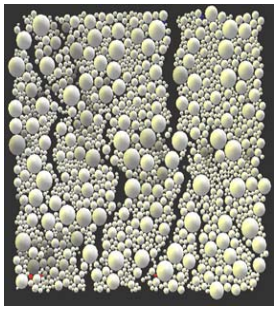

a)

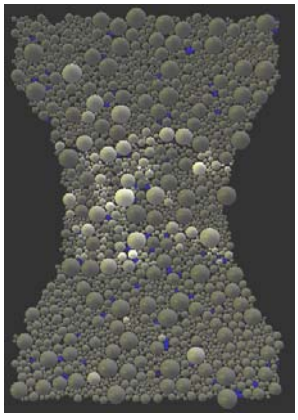

b)

Figure 5: Calculated fracture at failure of concrete specimens during uniaxial compression (a) and uniaxial tension (b) from discrete simulations.

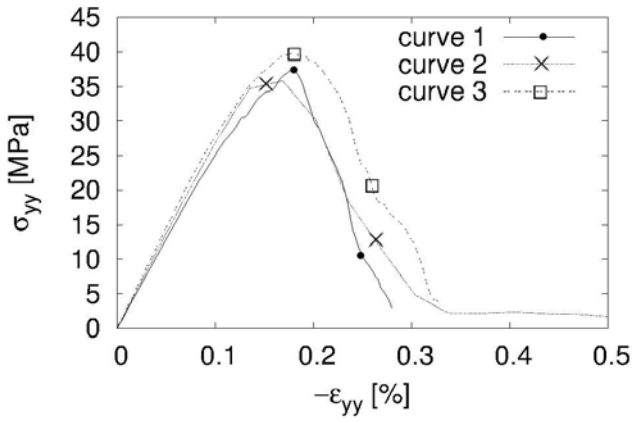

a)

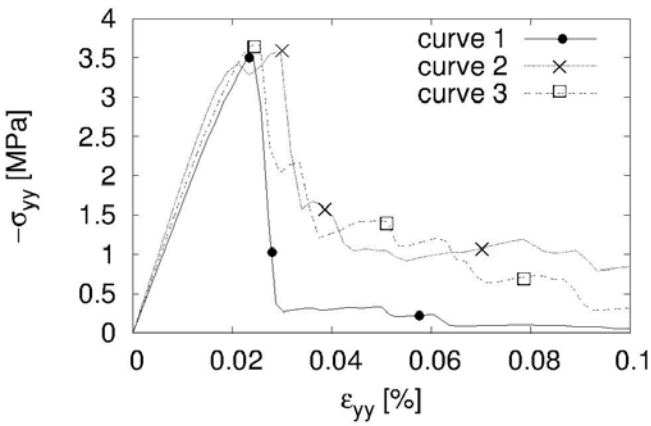

b)

Figure 6: Influence of mean aggregate diameter d_{50} on stress-strain diagram during uniaxial compression (a) and tension (b) from discrete simulations (curve '1' - d_{50}=4.5 mm, curve '2' - d_{50} =4.0 mm, curve '3' - d_{50}=3.0 mm).

5 OWN EXPERIMENTS

5.1 Experimental set-up

Three-point bending laboratory tests carried out on concrete beams of a different size $D \times L$ with free ends were carried out (D – beam height, L=4D – beam length) (Fig.8).

The beams were geometrically similar: small size beams 80×320 mm^2 medium size beams 160×640 mm^2 and large size beams 320×1280 mm^2. The beam thickness was always 40 mm. The beam span was equal to 3D. A notch of the height of D/10 mm and

width of 3 mm was located in the middle of each beam bottom. The geometry of the beams was the same as that assumed in laboratory tests by Le Bellĕgo et al. [14]. The tests were performed with a controlled notch opening displacement velocity (or crack mouth opening displacement CMOD rate) of 0.002 mm/min. This type of control allowed for obtaining a gradual displacement increase and a steady strength decrease in a post-peak regime. A CMOD gauge was located below the beam notch.

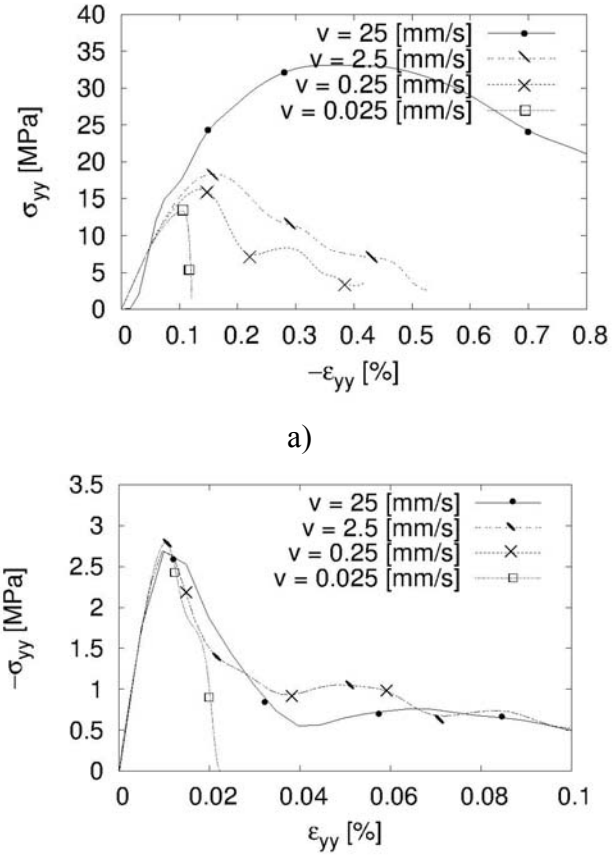

Figure 7: Influence of loading velocity on stress-strain diagram during compression (a) and tension (b) from discrete simulations.

Several different concrete mixes were composed of ordinary Portland cement (CEM II/B-S 32.5R), water and sand (mean aggregate diameter d_{50}=0.5 mm, maximum aggregate diameter d_{max}=2.0 mm) or gravel (mean aggregate diameter d_{50}=2.0 mm, maximum aggregate diameter d_{max}=16 mm). The water to cement ratio was 0.5. Two volumes of aggregate were assumed, namely 45% and 70%. Rounded-stone-shaped aggregate and crushed-stone-shaped aggregate were used. The beams were cut out from the same mix block. In experiments, the digital camera Canon EOS-1Ds Mark II with a powerful 16.7 megapixels CMOS sensor was applied. It was mounted on the tripod with its axis perpendicular to the photographed specimen surface. The concrete beams were initially carefully polished, then painted white. After that a spackle pattern (serving as a tracer) was put on this surface using the yellow spray. During the experiments, the width of FPZ was also measured with a CMOD gauge placed under the notch. The length resolution of images was 100 pixels/mm.

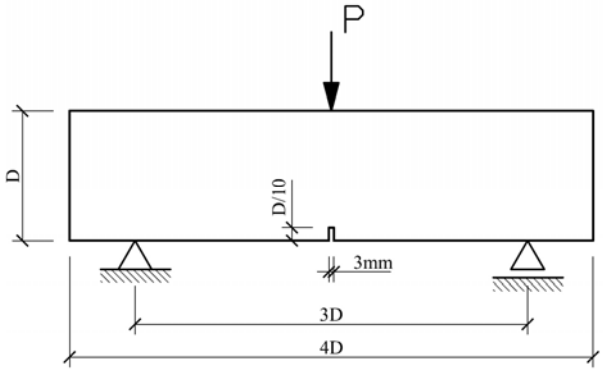

Figure 8: Geometry of experimental concrete notched beams subjected to three-point bending [4], [5].

5.2 Experimental results

A fracture process zone was always strongly curved and may even create branches (Fig.9). The measured width of FPZ changes between 3.55 mm in sand concrete ($\approx 1.75 \times d_{max}$) and 4.84 mm ($\approx 0.3 \times d_{max}$) in gravel concrete (with the volume of rounded-stone-shaped aggregate V=45%).

A localized zone was always created before the peak on the vertical force–horizontal CMOD diagram (Fig.10). It developed during a deformation process until a discrete macro-crack was created at the deflection of u/D=0.004.

The FPZ width (sand concrete, volume of rounded-stone shape aggregate 45%) increased due to concrete dilatancy up to w_c=3.55 mm in the range of CMOD=0.02-0.07 mm. Its formation rate was strongly non-linear caused be a heterogeneous concrete structure. The length and height of a localized zone above the notch were l_c=65 mm and h_c=46 mm (h_c/D=0.575) at CMOD≈0.07 mm, respectively (Fig.11).

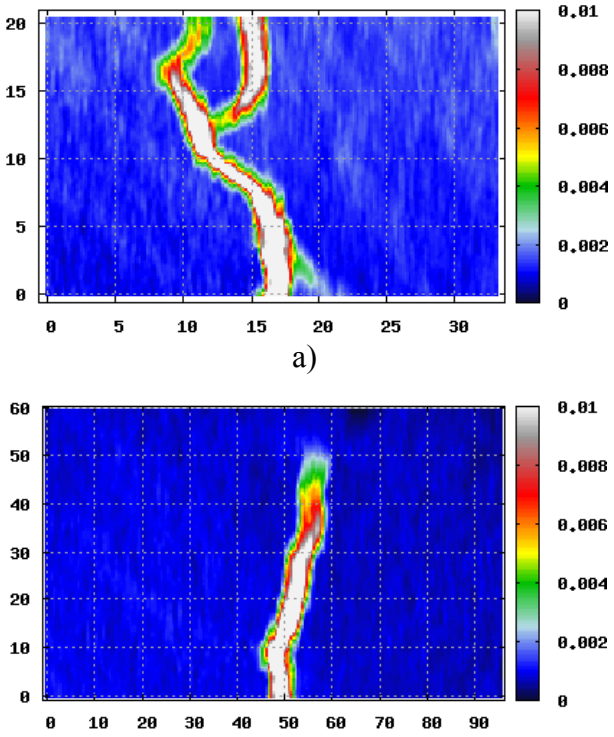

Figure 9: Localized zone directly above notch in experiments with concrete notched beams based on horizontal normal strain (vertical and horizontal axes denote coordinates in [mm] and colour scale strain intensity): a) sand concrete, b) gravel concrete

5.3 Size effect

Figure 12 shows a measured size effect for gravel concrete beams (d_{50}=2.0 mm, $d_{\max}$=16 mm, V=70%) geometrically similar. In addition, the results following the size effect law by Bažant [15] (being valid for structures of a similar geometry with pre-existing notches or large cracks) and experimental results by Le Bellĕgo et al. [14] were enclosed. All results have a similar trend.

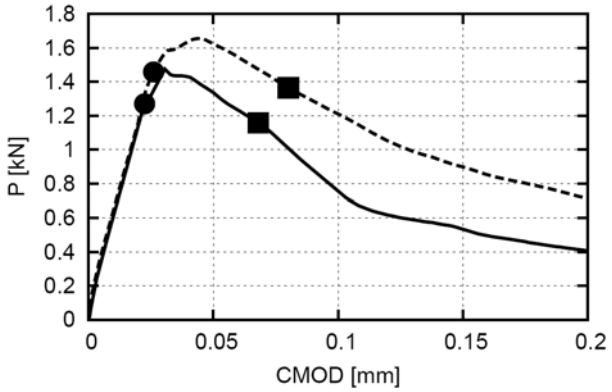

Figure 10: Formation of localized zone and macro-crack on vertical force P – CMOD diagram (● - appearance of localized zone, ■ - appearance of macro-crack)

6 CONCLUSIONS

The combined DEM-FEM computations with a numerically calculated tangent stiffness matrix provide realistic results for simple loading cases in spite of the occurrence of several unstable points. The results are similar to those obtained from DEM computations and qualitatively similar to the corresponding laboratory tests. They give certainly a faster response for large boundary value problems than DEM.

The DEM method is a reliable numerical tool for describing the meso-behaviour of concrete. It can be used for the detailed study of a fracture process at the aggregate level.

The Digital Image Correlation technique is a very effective optical technique to determine the displacement field on the surface of concrete with a high accuracy and without any physical contact with the surface.

The width and length of a localized zone on the concrete surface of notched beams non-uniformly increased during a deformation process before a macro-crack formed due to a heterogeneous concrete composition. The maximum width of a localized zone was 3.55 mm in a sand concrete beam (≈1.75×d_{max}) and 4.84 mm (≈0.3×d_{max}) in a gravel concrete beam at the length resolution of 100 pixels per

mm. The maximum ratio between the height of a localized zone and effective beam height was approximately 0.6. A macro-crack occurred in a softening regime for displacements about two times larger than at the peak load.

The nominal strength of notched concrete beams during three-point bending increased with decreasing beam height and beam span.

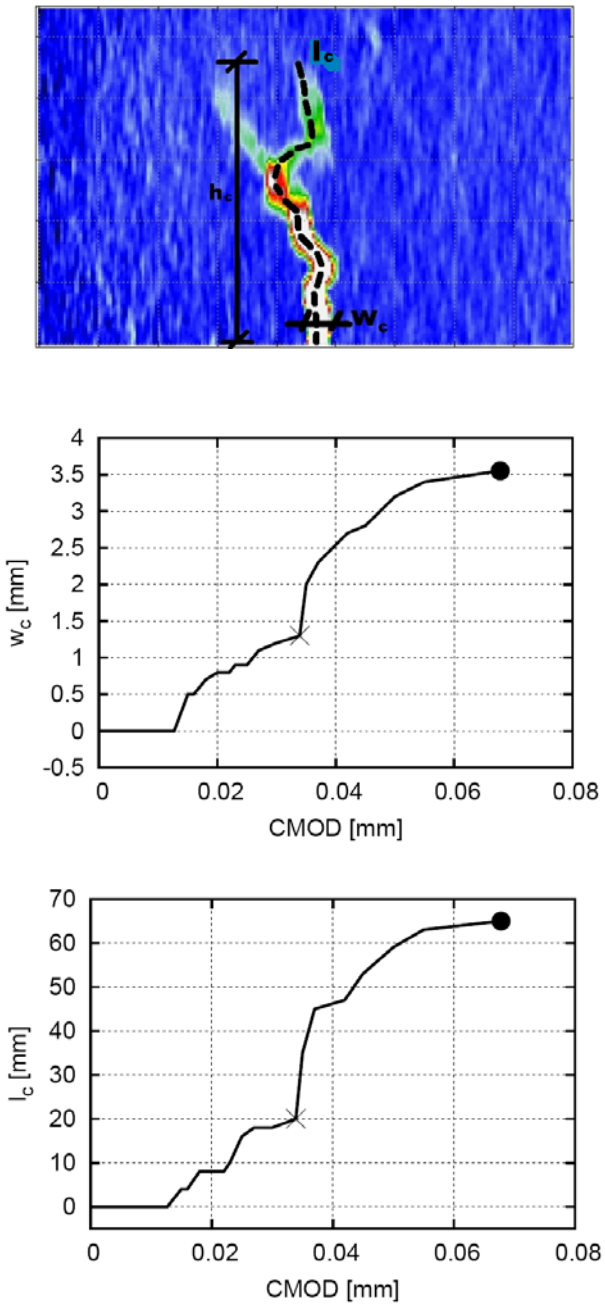

Figure 11: Evolution of width w_c and length l_c of localized zone against CMOD in experiments with notched beam of fine-grained concrete based on DIC (× - maximum vertical force P_{max}, • - formation of macro-crack)

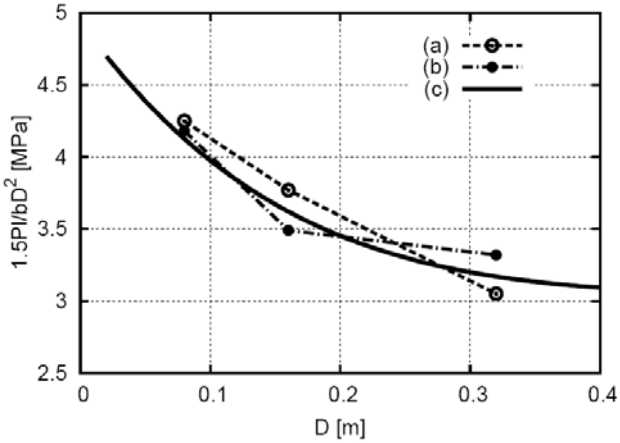

Figure 12: Calculated and measured size effect in nominal strength $1.5Pl/(bD^2)$ versus beam height D for concrete beams of a similar geometry: a) our laboratory experiments, b) experiments by Le Bellĕgo et al. [14], c) size effect law by Bažant [15].

7 ACKNOWLEDGEMENT

Research work has been carried out as a part of the project: "Innovative resources and effective methods of safety improvement and durability of buildings and transport infrastructure in the sustainable development" financed by the European Union (POIG.01.01.02-10-106/09-01).

REFERENCES

[1] Nitka, M., Combe, G., Dascalu, C. and Desrues, J., 2011. Two-scale modeling of granular materials: a DEM-FEM approach. *Granular Matter* **13**:277-281.

[2] Widuliński, Ł., Tejchman, J., Kozicki, J. and Leśniewska, D., 2011. Discrete simulations of shear zone patterning in sand in earth pressure problems of a retaining wall. *International Journals of Solids and Structures* **48**:1191-1209.

[3] Hill, R., 1963. Elastic properties of reinforced solids: Some theoretical

principles. *Journal of the Mechanics and Physics of Solids* **11**:357-372.

[4] Skarżyński, Ł, Syroka, E. and Tejchman, J., 2011. Measurements and calculations of the width of the fracture process zones on the surface of notched concrete beams. *Strain* **47**:319-332.

[5] Skarżyński, Ł. and Tejchman, J., 2010. Calculations of fracture process zones on meso-scale in notched concrete beams subjected to three-point bending. *European Journal of Mechanics/A Solids* **29**:746-760.

[6] Cundall, P.A. and Strack, O.D.L., 1979. A discrete numerical model for granular assemblies. *Geotechnique* **29**, 1:47-65.

[7] Skarżyński, Ł. and Tejchman, J., 2012. Determination of representative volume element in concrete under tensile deformation. *Computers and Concrete* **1**, 9:35-50.

[8] Bonnet, J. and Wood, R.D., 1997. Nonlinear continuum mechanics for finite element analysis. *Cambridge University Press,* pp. 53-117.

[9] Nitka, M., Combe, G., Dascalu, D. and Desrues, J. 2010. A multi scale approach to geotechnical problems of granular systems: a DEM-FEM combination. *Report of Ecole Nationale des Ponts et Chaussees.*

[10] Kozicki, J. and Donze, F.V., 2008. A new open-source software developed for numerical simulations using discrete modelling methods. *Computer Methods in Applied Mechanics and Engineering* **197**:4429-4443.

[11] Kozicki, J., Tejchman, J. and Mróz, Z., 2012. Effect of grain roughness on strength, volume changes, elastic and dissipated energies during quasi-static homogeneous triaxial compression using DEM. *Granular Matter* **14**, 4:457-468.

[12] van Mier, J.G.M., 1986. Multiaxial strain-softening of concrete. *Materials & Structures* **19**, 111: 179-200.

[13] van Vliet, M.R.A., van Mier, J.G.M., 2000. Experimental investigation of size effect in concrete and sandstone under uniaxial tension. *Engineering Fracture Mechanics* **65**, 165-188.

[14] Le Belléğo, C., Dube, J. F., Pijaudier-Cabot, G. and Gerard, B., 2003. Calibration of nonlocal damage model from size effect tests. *European Journal of Mechanics A/Solids* **22**:33-46.

[15] Bažant, Z. and Planas, J., 1998. *Fracture and size effect in concrete and other quasi-brittle materials.* CRC Press LLC.